THE JOURNAL OF PHYSICAL CHEMISTRY C

Article

pubs.acs.org/JPCC

Mechanical Modeling of Particles with Active Core–Shell Structures for Lithium-Ion Battery Electrodes

Bin Wu and Wei Lu*

Department of Mechanical Engineering, University of Michigan, Ann Arbor, Michigan 48109, United States

Supporting Information

ABSTRACT: Active particles with a core–shell structure exhibit superior physical, electrochemical, and mechanical properties over their single-component counterparts in lithium-ion battery electrodes. Modeling plays an important role in providing insights into the design and utilization of this structure. However, previous models typically assume a shell without electrochemical activity. Inaccurate interfacial conditions have been used to bridge the core and the shell in several studies. This work develops a physically rigorous model to describe the diffusion and stress inside the core–shell structure based on a generalized chemical potential. Including both chemical and mechanical effects, the generalized chemical potential governs the diffusion in both the shell and the core. The stress is calculated using the lithium concentration profile. Our simulations reveal a lithium concentration jump forming at the core–shell interface, which is only possible to capture by modeling the shell as electrochemically active. In sharp contrast to a single-component particle, a tensile radial stress develops at the core–shell interface during delithiation, while a tensile tangential stress develops in the shell during lithiation. We find that the core–shell interface is prone to debonding for particles with a thick shell, while shell fracture is more likely to occur for particles with a large core and a relatively thin shell. We show a design map of the core and shell sizes by considering both shell fracture and shell debonding.

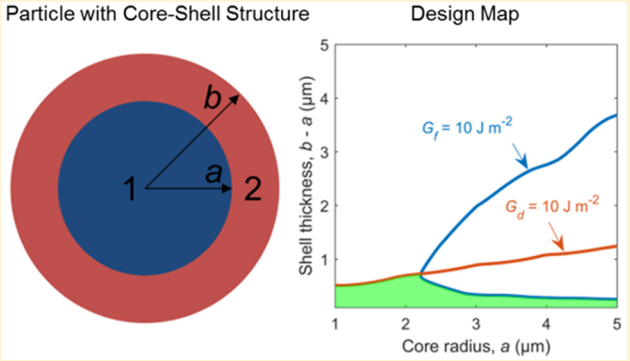

1. INTRODUCTION

The growing demand for higher energy density and power density, longer cycle life, and lower cost of lithium ion batteries has driven significant progress in battery materials research. Besides searching for new materials, engineering of material structure is equally important to fully exploit the potential of existing or new materials. Core–shell structure is an effective strategy to combine the advantages and avoid the disadvantages of two materials.[1] For example, cathode active particles with a $LiNi_{0.8}Co_{0.1}Mn_{0.1}$ core and a $LiNi_{0.5}Mn_{0.5}$ shell structure have been synthesized,[2,3] where the Ni-rich core delivers high capacity, while the Mn-rich shell improves the thermal and structural stabilities. The core–shell structure has also been used for anode materials. The silicon particle, which has a high theoretical capacity, suffers from dramatic volume change during lithiation/delithiation processes. Researchers have proposed to coat a layer of carbon[4] or silicon oxide[5] to restrict the volume change of silicon, thus to improve the cycle life. In addition to these purposely designed core–shell structures, passively formed core–shell structures can also be found in battery materials, such as the solid electrolyte interface (SEI) film forming at the surface of an active particle. Overall, in a core–shell structure the shell can (1) protect the core from environmental corrosion or side reactions, such as the SEI film on the surface of a graphite particle,[6] (2) enhance physical or chemical properties, such as the carbon shell outside a Mn_2O_4 core to improve the conductivity,[7] or (3) restrict the volume change of the core to maintain structural integrity, such as the carbon shell outside a silicon core.[8]

Stress generation associated with solid diffusion has been widely discussed in the literature. Researchers have investigated the mechanical and electrochemical behaviors of a single particle with a three-dimensional morphology[9] and a secondary particle with an agglomerate structure.[10] The developed stress inside the particle brings two effects. The first effect is the influence of stress on degradation in the core–shell structure. For the core–shell structure, the resulting stress from the lithium diffusion may lead to fracture of the shell or debonding between the core and the shell. For instance, a large void has been observed to form at the interface of the $LiNi_{0.8}Co_{0.1}Mn_{0.1}$ core and the $LiNi_{0.5}Mn_{0.5}$ shell after long-term cycling, owing to the structural mismatch and the difference in volume change between the core and the shell.[11] Similarly, the expansion of a lithiated graphite core can lead to fracture of the SEI film, which further causes solvent decomposition and capacity degradation.[12]

The second effect is the influence of stress on electrochemistry in the core–shell structure. Mechanical stress can change the electrochemical potential of solids and therefore affects the

Received: May 25, 2017
Revised: August 7, 2017
Published: August 11, 2017

DOI: 10.1021/acs.jpcc.7b05096
J. Phys. Chem. C 2017, 121, 19022–19030

diffusion[9] or lithiation processes[13,14] inside the particle. For example, the developed stress gradient inside a $LiMn_2O_4$ particle is predicted to increase the effective solid diffusivity by up to 35%.[9] Calculations have shown that the pressure generated from the shell can halt the lithiation process inside the core.[13] The plastic deformation of amorphous silicon accounts for a significant percentage of the energy dissipated during the cycling at low C-rates.[15]

Modeling the core−shell structure has attracted significant attention recently.[6,7,12−14,16] However, current models typically treat the shell as mechanical constraint only without any electrochemical activity.[12,13,16] In this treatment, the lithium ions directly insert into or extract from the core without moving across the shell, which is not consistent with physical reality. In one work,[7] although the diffusion through the carbon shell is modeled, the associated expansion inside the shell is neglected. Moreover, the assumption that the lithium concentration is continuous through the core−shell interface often cannot be satisfied since the core and shell are two phases with distinct affinity for lithium. Physically, a more natural way to tackle the diffusion in multiple phases is to use the chemical potential instead of the concentration. As mechanical stress resulting from concentration gradient can affect the chemical potential, modeling the core−shell structure requires fully coupling mechanics and electrochemistry.

In this work, we develop a physically rigorous model to describe lithium diffusion and the resulting stress generation inside a particle with a core−shell structure. The generated stress and its effect on debonding between the core and the shell or shell fracture are correlated to the design parameters of the core−shell structure. Using the energy release rate, a design map is developed to guide the synthesis and application of the core−shell structure.

2. MODEL DEVELOPMENT

Figure 1 shows the schematic of the model, where phase 1 denotes the core with a radius of a and phase 2 denotes the shell

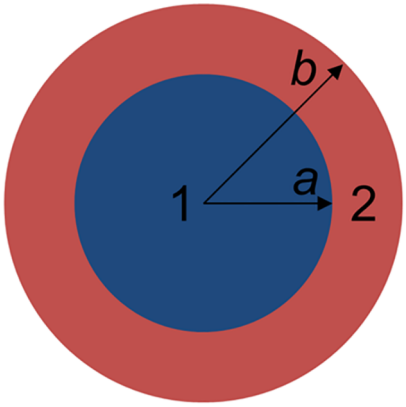

Figure 1. Schematic of the core−shell structure.

with an outer radius of b. Both the core and the shell are electrochemically active for lithiation and delithiation, and both undergo volume change.

2.1. Electrochemistry. The lithium concentration in the particle, c, either in the core or in the shell, is governed by

$$\frac{\partial c}{\partial t} + \nabla\cdot\mathbf{J} = 0 \tag{1}$$

The flux of lithium ions, $\mathbf{J}$, is given by[21]

$$\mathbf{J} = -Mc\nabla\mu \tag{2}$$

where M is the lithium mobility in the solid and μ is the chemical potential of lithium in the active particle. A discussion of the rigorous definition of the chemical potential can be found in the Supporting Information.

Taking into account the effect of mechanical stress, the chemical potential of the lithium ion in the active particle is given by

$$\mu = \mu_c + \mu_m \tag{3}$$

where μ_c denotes the chemical potential at the stress-free state and μ_m denotes the effect of mechanical stress on the chemical potential.

The expression of μ_m has been discussed in several works.[17−20] Under the assumption of small linear elastic deformation and no dependence of mechanical properties on lithium fraction, eq 3 can be written as[9]

$$\mu = \mu_c - \Omega\sigma_h \tag{4}$$

where Ω is the partial molar volume of lithium ion in the active particle and σ_h is the hydrostatic stress in the particle.

Explicit expressions of μ_c can be found in the literature.[9,21] However, since it is the gradient of the chemical potential, rather than the chemical potential itself, that drives diffusion, the explicit expression of the chemical potential is not crucial for the diffusion equation. When substituting eq 4 into eq 2, the flux is given by

$$\mathbf{J} = -Mc\left(\frac{\partial\mu_c}{\partial c}\nabla c - \Omega\nabla\sigma_h\right) \tag{5}$$

The open circuit potential (with respect to lithium metal) of the active particle, E_{ref}, depends on the difference in chemical potential between a lithium metal (μ^θ) and the active particle (μ)

$$E_{ref} = \frac{\mu^\theta - \mu_c}{F} \tag{6}$$

where F is the Faraday constant. Then, the term $\partial\mu_c/\partial c$ can be determined through the profile of the open circuit potential as

$$\frac{\partial\mu_c}{\partial c} = -F\frac{\partial E_{ref}}{\partial c} = -\frac{F}{c_{max}}\frac{\partial E_{ref}}{\partial x_{Li}} = -\frac{FK}{c_{max}} \tag{7}$$

where c_{max} is the maximum lithium concentration in the solid, x_{Li} is the lithium fraction inside the active material, and $K = \partial E_{ref}/\partial x_{Li}$ is called the thermodynamic factor in this work.

Given that the lithium ion diffusion in the active material occurs by a vacancy mechanism, the mobility decreases with the increase of lithium concentration. With this consideration, the mobility can be expressed by[21]

$$M = M_0\left(1 - \frac{c}{c_{max}}\right) \tag{8}$$

where $M_0 = D_0/RT$ is the lithium ion mobility in the solid, D_0 is diffusivity, R is gas constant, and T is absolute temperature.

Combining eqs 2−8 and considering the symmetry of a spherical particle, we can obtain that the flux of lithium ions is along the radial direction, r, of the particle, which is given by

$$J = \frac{D_{eff}}{RT}\left(FK\frac{\partial c}{\partial r} + \Omega c_{max}\frac{\partial\sigma_h}{\partial r}\right) = J_c + J_m \tag{9}$$

DOI: 10.1021/acs.jpcc.7b05096
J. Phys. Chem. C 2017, 121, 19022−19030

where $D_{\text{eff}} = D_0\left(1 - \frac{c}{c_{\max}}\right)\left(\frac{c}{c_{\max}}\right)$ is the effective diffusivity, $J_c = \frac{D_{\text{eff}}FK}{RT}\frac{\partial c}{\partial r}$ is the chemically driven flux, and $J_m = \frac{D_{\text{eff}}\Omega c_{\max}}{RT}\frac{\partial \sigma_h}{\partial r}$ is the mechanically driven flux.

Equation 1 takes the form of $\partial c/\partial t + (1/r^2)\partial(r^2 J)/\partial r = 0$ in the spherical coordinate. Solving this equation together with eq 9 gives the concentration field in the core and in the shell. In the following, we use subscripts 1 and 2 to denote the field in the core and in the shell, respectively.

Prior models assume that the lithium concentration is continuous across the phase interface, i.e., $c_1(r = a) = c_2(r = a)$.[7] However, as the core and the shell have different affinity for the lithium, a more rigorous expression to bridge the two regions is using the chemical potential

$$\mu_1(r = a) = \mu_2(r = a) \tag{10}$$

We have transformed this boundary condition to an equation that relates the concentration and stress fields in the core and in the shell. The derivation can be found in the Supporting Information.

The lithium flux is continuous across the phase interface

$$J_1(r = a) = J_2(r = a) \tag{11}$$

The boundary conditions are given by

$$r = 0: \frac{\partial c_1}{\partial r} = 0$$

$$r = b: J_2 = \frac{i_{\text{app}}}{Fa_s L} \tag{12}$$

where i_{app} is the applied current density on the electrode in the unit of A m^{-2}, $a_s = 3\varepsilon_s/b$ is the active surface area per unit electrode volume, ε_s is the volume fraction of active solid particles in the electrode, and L is the electrode thickness. Note that we define $i_{\text{app}} < 0$ for intercalation and $i_{\text{app}} > 0$ for deintercalation.

The initial conditions are given by

$$t = 0: c_1 = c_{1,0},\ c_2 = c_{2,0} \tag{13}$$

The initial concentration of the two phases should satisfy equal chemical potential, i.e., $t = 0$: $\mu_1 = \mu_2$.

The solid diffusion inside the particle can be coupled with the electrode level behavior using the single particle model.[22] The cell voltage with respect to a lithium reference electrode is given by

$$V = E_{\text{ref},2}(c_2(r = b)) + \frac{2RT}{F}\ln\left(\frac{\sqrt{m^2 + 4} + m}{2}\right) + i_{\text{app}}R_{\text{sol}} \tag{14}$$

where $m = \frac{i_{\text{app}}}{Fa_s L k c_e^{0.5}(c_{2,\max})^{0.5}(c_{2,\max} - c_2(r = b))^{0.5}}$, k is the reaction rate constant of the shell material, c_e is the lithium ion concentration in the electrolyte, and R_{sol} is the electrolyte resistance in the unit of Ω m^2.

2.2. Mechanics. Stress equilibrium, either in the core or in the shell, is given by

$$\frac{\partial \sigma_{rr}}{\partial r} + 2\frac{\sigma_{rr} - \sigma_{\theta\theta}}{r} = 0 \tag{15}$$

where σ_{rr} is the radial stress and $\sigma_{\theta\theta}$ is the tangential stress.

The strain components are written as functions of the displacement

$$\varepsilon_{rr} = \frac{\mathrm{d}u}{\mathrm{d}r},\ \varepsilon_{\theta\theta} = \frac{u}{r} \tag{16}$$

where ε_{rr} is the radial strain, $\varepsilon_{\theta\theta}$ is the tangential strain, and u is the radial displacement.

The relations between stress and strain are given by

$$\sigma_{rr} = \frac{E}{(1 + \nu)(1 - 2\nu)}\left[(1 - \nu)\varepsilon_{rr} + 2\nu\varepsilon_{\theta\theta} - (1 + \nu)\frac{\Omega\tilde{c}}{3}\right]$$

$$\sigma_{\theta\theta} = \frac{E}{(1 + \nu)(1 - 2\nu)}\left[\nu\varepsilon_{rr} + \varepsilon_{\theta\theta} - (1 + \nu)\frac{\Omega\tilde{c}}{3}\right] \tag{17}$$

where E is Young's modulus, ν is Poisson's ratio, Ω is the partial molar volume of lithium ion in the active particle, $\tilde{c} = c - c_0$ is the difference between lithium concentration at the current state, c, and the initial stress-free state, c_0.

When substituting eqs 16 and 17 into eq 15, the radial displacement is governed by

$$\frac{\mathrm{d}}{\mathrm{d}r}\left(\frac{1}{r^2}\frac{\mathrm{d}}{\mathrm{d}r}(r^2 u)\right) = \frac{1 + \nu}{1 - \nu}\frac{\Omega}{3}\frac{\mathrm{d}\tilde{c}}{\mathrm{d}r} \tag{18}$$

We use the subscript 1 and 2 to denote the field in the core and in the shell, respectively. The solutions of eq 18 in the core and in the shell take the forms of

$$\text{in the core } (0 \le r \le a): u_1 = A_1 r + \frac{B_1}{r^2} + \frac{(1 + \nu_1)}{3(1 - \nu_1)}\frac{\Omega_1}{r^2}\int_0^r \tilde{c}_1 r^2\,\mathrm{d}r \tag{19}$$

$$\text{in the shell } (a \le r \le b): u_2 = A_2 r + \frac{B_2}{r^2} + \frac{(1 + \nu_2)}{3(1 - \nu_2)}\frac{\Omega_2}{r^2}\int_a^r \tilde{c}_2 r^2\,\mathrm{d}r \tag{20}$$

where A_1, B_1, A_2, and B_2 are constants to be determined by the continuity conditions and the boundary conditions. The continuity of displacement and radial stress at the interface between the core and the shell is given by

$$u_1(r = a) = u_2(r = a)$$

$$\sigma_{rr,1}(r = a) = \sigma_{rr,2}(r = a) \tag{21}$$

The boundary conditions are given by

$$u_1(r = 0) = 0$$

$$\sigma_{rr,2}(r = b) = 0 \tag{22}$$

By substituting eqs 19 and 20) into eqs 16 and 17, and further into eqs 21 and 22, we can solve for A_1, B_1, A_2, and B_2 and obtain the stress and displacement fields in the core and in the shell as shown below.

The radial stress at the core−shell interface, σ_{rr}^{cs}

DOI: 10.1021/acs.jpcc.7b05096
J. Phys. Chem. C 2017, 121, 19022−19030

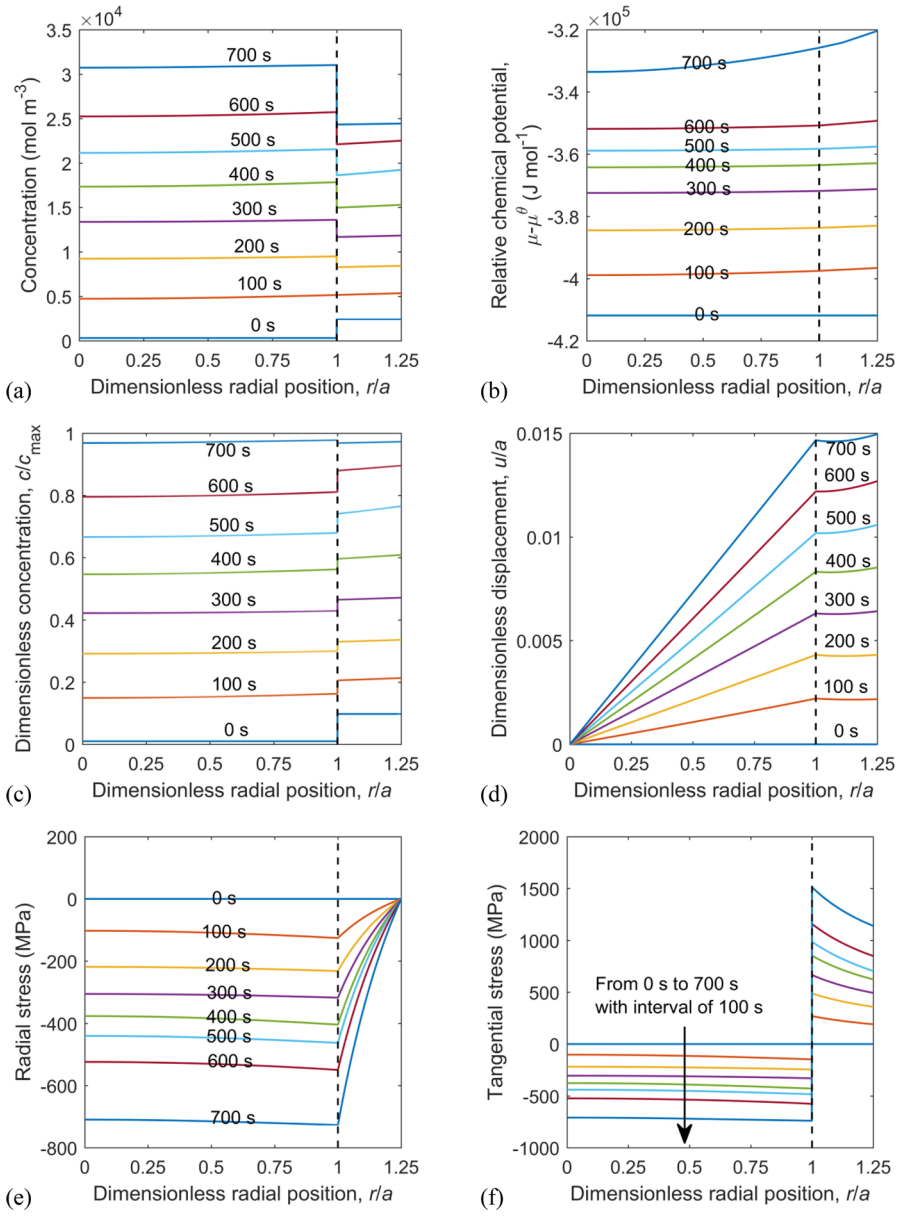

Figure 2. Radial distribution of (a) concentration, (b) relative chemical potential, (c) dimensionless concentration, (d) dimensionless displacement, (e) radial stress, and (f) tangential stress at eight times during lithium intercalation. The dimensionless concentration is defined with respect to the maximum concentration of the core and of the shell, respectively. The relative chemical potential is defined as $\mu - \mu^{\theta}$, where μ^{θ} is the chemical potential of lithium in lithium metal. The vertical dash line represents the core−shell interface. In this simulation, $a = 4$ μm, $b = 5$ μm, and $i_{app} = -100$ A m^{-2}.

$$\sigma_{rr}^{cs} = \frac{2E_1E_2}{a^3}\frac{\Omega_2\int_a^b \tilde{c}_2 r^2\,\mathrm{d}r - \left[\left(\frac{b}{a}\right)^3 - 1\right]\Omega_1\int_0^a \tilde{c}_1 r^2\,\mathrm{d}r}{\left(\frac{b}{a}\right)^3[E_1(1+\nu_2) + 2E_2(1-2\nu_1)] + 2[E_1(1-2\nu_2) - E_2(1-2\nu_1)]} \tag{23}$$

In the core $(0 \le r \le a)$:

$$\sigma_{rr,1} = \sigma_{rr}^{cs} + \frac{2\Omega_1E_1}{3(1-\nu_1)}\left(\frac{1}{a^3}\int_0^a \tilde{c}_1 r^2\,\mathrm{d}r - \frac{1}{r^3}\int_0^r \tilde{c}_1 r^2\,\mathrm{d}r\right) \tag{24}$$

$$\sigma_{\theta\theta,1} = \sigma_{rr}^{cs} + \frac{\Omega_1E_1}{3(1-\nu_1)}\left(\frac{2}{a^3}\int_0^a \tilde{c}_1 r^2\,\mathrm{d}r + \frac{1}{r^3}\int_0^r \tilde{c}_1 r^2\,\mathrm{d}r - \tilde{c}_1\right) \tag{25}$$

$$u_1 = \frac{r(1-2\nu_1)\sigma_{rr}^{cs}}{E_1} + \frac{r\Omega_1}{3}\left[\frac{2(1-2\nu_1)}{1-\nu_1}\frac{1}{a^3}\int_0^a \tilde{c}_1 r^2\,\mathrm{d}r + \frac{1+\nu_1}{1-\nu_1}\frac{1}{r^3}\int_0^r \tilde{c}_1 r^2\,\mathrm{d}r\right] \tag{26}$$

In the shell $(a \le r \le b)$:

DOI: 10.1021/acs.jpcc.7b05096
J. Phys. Chem. C 2017, 121, 19022−19030

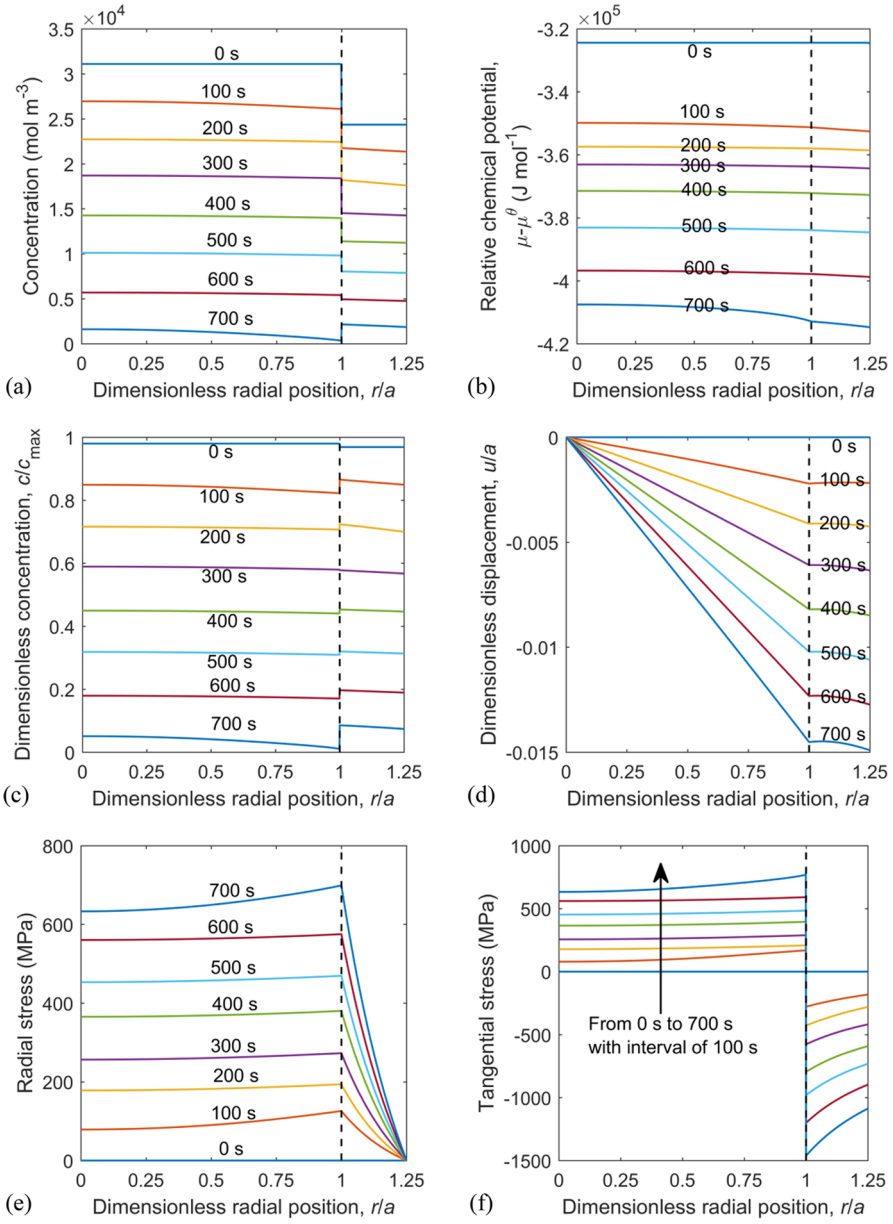

Figure 3. Radial distribution of (a) concentration, (b) relative chemical potential, (c) dimensionless concentration, (d) dimensionless displacement, (e) radial stress, and (f) tangential stress at eight times during lithium deintercalation. The dimensionless concentration is defined with respect to the maximum concentration of the core and of the shell, respectively. The relative chemical potential is defined as $\mu - \mu^{\theta}$, where μ^{θ} is the chemical potential of lithium in lithium metal. The vertical dash line represents the core−shell interface. In this simulation, a = 4 μm, b = 5 μm, and i_{app} = 100 A m^{-2}.

$$\sigma_{rr,2} = \frac{a^3}{b^3 - a^3}\left[\left(\frac{b}{r}\right)^3 - 1\right]\sigma_{rr}^{cs} + \frac{2\Omega_2 E_2}{3(1-\nu_2)} \left[\frac{1}{b^3 - a^3}\left(1 - \left(\frac{a}{r}\right)^3\right)\int_a^b \tilde{c}_2 r^2\, dr - \frac{1}{r^3}\int_a^r \tilde{c}_2 r^2\, dr\right] \quad (27)$$

$$\sigma_{\theta\theta,2} = -\frac{a^3}{b^3 - a^3}\left[1 + \frac{1}{2}\left(\frac{b}{r}\right)^3\right]\sigma_{rr}^{cs} + \frac{\Omega_2 E_2}{3(1-\nu_2)} \left[\frac{1}{b^3 - a^3}\left(2 + \left(\frac{a}{r}\right)^3\right)\int_a^b \tilde{c}_2 r^2\, dr + \frac{1}{r^3}\int_a^r \tilde{c}_2 r^2\, dr - \tilde{c}_2\right] \quad (28)$$

$$u_2 = -\frac{ra^3}{(b^3 - a^3)E_2}\left[(1-2\nu_2) + \frac{1}{2}\left(\frac{b}{r}\right)^3(1+\nu_2)\right]\sigma_{rr}^{cs} + \frac{r\Omega_2}{3}\left[\frac{1}{b^3 - a^3}\left(\frac{2(1-2\nu_2)}{1-\nu_2} + \frac{1+\nu_2}{1-\nu_2}\left(\frac{a}{r}\right)^3\right)\int_a^b \tilde{c}_2 r^2\, dr + \frac{1+\nu_2}{1-\nu_2}\frac{1}{r^3}\int_a^r \tilde{c}_2 r^2\, dr\right] \quad (29)$$

2.3. Parameters. In this work, the core is assumed to be $LiNi_{0.8}Mn_{0.1}Co_{0.1}O_2$ (NMC 811), while the shell is assumed to be $LiNi_{0.4}Mn_{0.4}Co_{0.2}O_2$ (NMC 442). The Ni-rich core is designed to provide high energy density, while the Mn-rich shell is used to improve the stability.

DOI: 10.1021/acs.jpcc.7b05096
J. Phys. Chem. C 2017, 121, 19022−19030

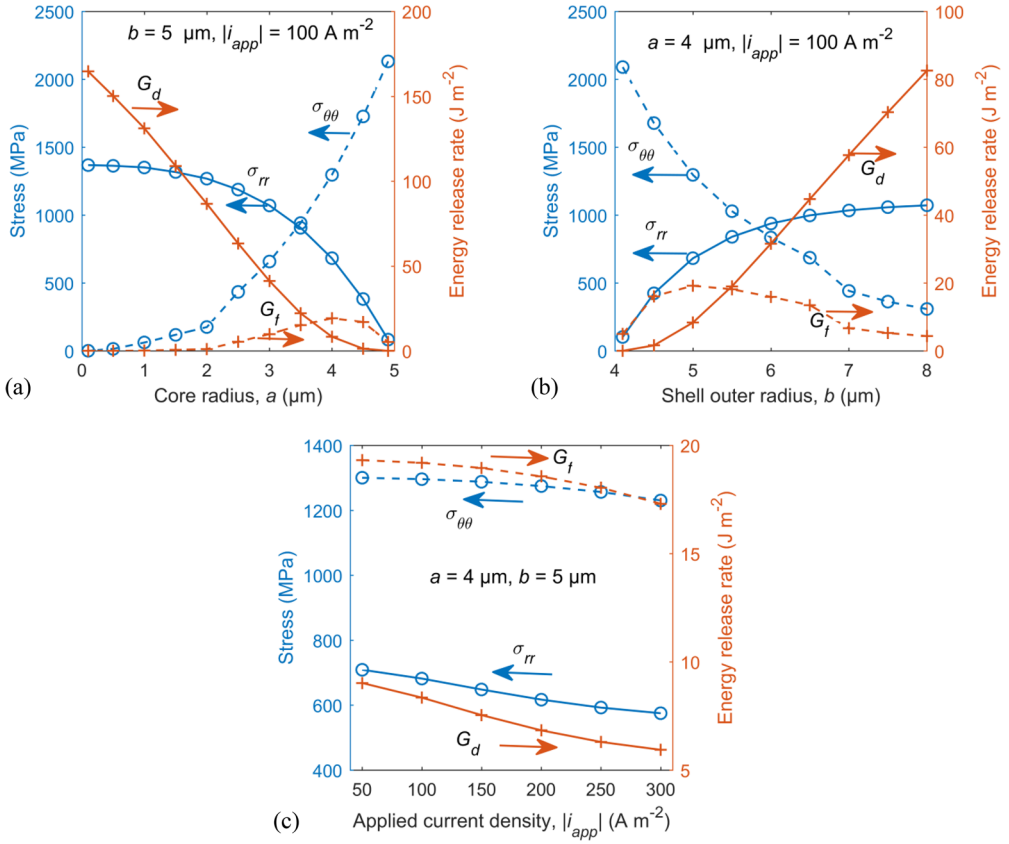

Figure 4. (a) Effect of core radius on stress and energy release rate under constant outer shell radius and magnitude of current density. (b) Effect of outer shell radius on stress and energy release rate under constant core radius and magnitude of current density. (c) Effect of the magnitude of current density on stress and energy release rate under constant core radius and outer shell radius. For all results, $\sigma_{\theta\theta}$ denotes the maximum average tangential stress of the shell during lithium intercalation, G_f denotes the fracture energy release rate at the time when $\sigma_{\theta\theta}$ reaches maximum, σ_{rr} denotes the maximum radial stress at the core−shell interface during lithium deintercalation, and G_d denotes the debonding energy release rate at the time when σ_{rr} reaches maximum.

The open circuit potential,[23,24] thermodynamic factor as functions of lithium fraction, diffusivity,[25] partial molar volume,[26,27] and maximum lithium concentration, and mechanical properties[28] of the core and of the shell can be found in Supporting Information.

3. RESULTS AND DISCUSSION

Simulation results of lithium intercalation are shown in Figure 2. Figure 2a shows the lithium concentration along the particle radius. A concentration jump can be observed at the core−shell interface, which results from the material difference (i.e., maximum lithium concentration and open circuit potential) between the core and the shell. Initially, the lithium concentration of the shell is much higher than the core as required by the equilibrium of chemical potential between the core and the shell. As lithiation proceeds, the concentration jump evolves to ensure a continuous chemical potential across the interface, as shown in Figure 2b. Note that the chemical potential here includes both the chemical and the mechanical effects. Figure 2c shows the dimensionless concentration normalized by the maximum concentration of the core and of the shell, respectively. The dimensionless concentration jump gradually vanishes since the OCV difference between the core and the shell decreases as the dimensionless concentration approaches to 1.

The radial displacement associated with lithiation is shown in Figure 2d. The shell has a smaller gradient of radial displacement or radial strain than the core. The shell swells less than the core because (1) the shell has a smaller partial molar volume than the core, as listed in the Supporting Information; and (2) the lithium concentration change of the shell is smaller than the core, as shown in Figure 2a. Thus, the shell restricts the expansion of the core to a certain extent. Also, note that the dimensionless displacement is small, showing that the elastic assumption is acceptable.

The effect of the shell restriction is illustrated by the compressive radial stress shown in Figure 2e. Generally, the particle with a single component undergoes tensile radial stress during lithiation. However, the core−shell structure exhibits a compressive radial stress. This opposite mechanical behavior is understandable considering the constraining effect by the shell. To balance the radial stress, the tangential stress has a distribution as shown in Figure 2f. Note that the tangential stress is discontinuous across the core−shell interface. The tensile tangential stress in the shell may lead to shell fracture.

Simulation results of lithium deintercalation are shown in Figure 3. Similar to lithium intercalation, a larger concentration change occurs in the core than that in the shell. Consequently, the shell hampers the contraction of the core, resulting in a large radial stress at the core−shell interface. This radial stress may cause debonding between the core and the shell.

As discussed above, two possible failure modes exist in the core−shell structure. To quantify the relation between stress and failure modes, we use the energy release rate defined in fracture mechanics. The energy release rate of shell fracture is given by[14]

DOI: 10.1021/acs.jpcc.7b05096
J. Phys. Chem. C 2017, 121, 19022−19030

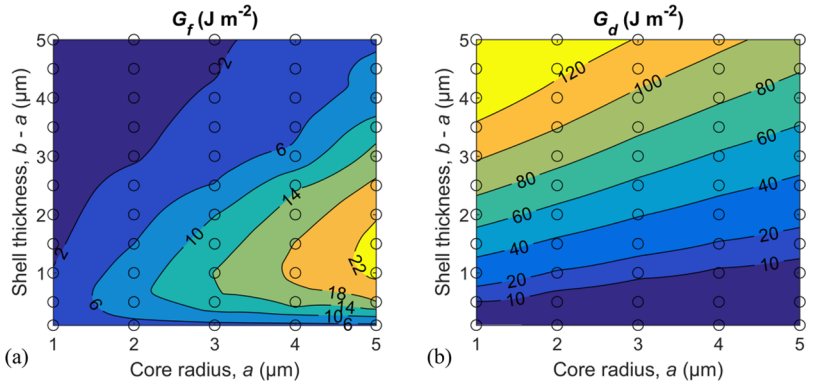

Figure 5. (a) Effect of core radius and shell thickness on fracture energy release rate. (b) Effect of core radius and shell thickness on debonding energy release rate. For all simulation results, the magnitude of current density is 100 A m^{-2}. The black dots represent the sampling points for simulations. The contour is generated based on the results of sampling points using natural neighbor interpolation method. The smallest shell thickness calculated is 0.1 μm.

$$G_f = Z\frac{(\bar{\sigma}_{\theta\theta,2})^2}{E_2}(b - a) \tag{30}$$

where $\bar{\sigma}_{\theta\theta,2} = (2\int_a^b \sigma_{\theta\theta,2} r\, dr)/(b^2 - a^2)$ is the average tangential stress in the shell, and $Z = 2$ is a dimensionless parameter for a channel crack in a spherical shell.

The energy release rate of core−shell debonding is given by[14]

$$G_d = \pi\frac{(\sigma_{rr}^{cs})^2}{E_e}(b - a) \tag{31}$$

where the effective Young's modulus, E_e, is calculated by $1/E_e = (1/E_1 + 1/E_2)/2$. The energy release rate is a quadratic function of the radial stress at the core−shell interface, σ_{rr}^{cs}.

With the developed model and energy release rates, we have investigated the effect of design and operational parameters on the mechanics of core−shell structures. The shell can fail by fracture or debonding. When this happens, all the benefit from the shell would be lost. Therefore, it is important to identify the parameter windows to avoid shell failure. Figure 4a shows the effect of core radius on the stress and energy release rate under constant outer shell radius and magnitude of current density. With an increase in the core radius, the tensile tangential stress in the shell grows rapidly because the shell confining the core expansion becomes thinner. The fracture energy release rate, G_f, depends on both the tangential stress and the shell thickness. It increases and then decreases with the core radius, reaching a maximum at around $a = 4$ μm. In contrast, the debonding energy release rate, G_d, which depends on both the radial stress and the shell thickness, decreases with the core radius.

Figure 4b shows that the tangential stress decreases with the outer shell radius, while the radial stress increases with outer shell radius, when all other parameters are kept the same. G_f reaches a maximum at around $b = 5$ μm, while G_d grows rapidly with b.

For a particle of single component, high current density results in a large concentration gradient and therefore a large stress associated with the large concentration gradient. In contrast, the stress in the shell slightly decreases with the current density for a core−shell structure, as shown in Figure 4c. The reason is the following. The stress inside the shell develops primarily from the difference between the concentration in the core and that in the shell. Comparing with the large concentration jump across the interface of the core and the shell, the concentration within the core and the shell are relatively uniform, as shown in Figures 2a and 3a. Under a higher current density, less lithium ions intercalate into or deintercalate from the particle, when discharging or charging terminates with the voltage hitting the lower or upper threshold. Thus, the volume change of the core and the resulted shell stress decrease with the current density.

Using this model, we have systematically investigated the effect of core and shell sizes on failure. As shown in Figure 5a, large G_f occurs for a particle with a large core and a moderately thin shell. However, G_d mainly depends on the shell thickness and slightly decreases with the core radius. We can also find that G_d is generally much larger than G_f. This observation suggests that core−shell debonding may be the major failure mode for the core−shell structure where the critical energy release rate of core−shell debonding is close to or less than the critical energy release rate of shell fracture.

One application of the contours in Figure 5 is to guide the particle design. To demonstrate the idea, we assume that the critical energy release rates for shell fracture and shell debonding are both 10 J m^{-2}. Then a feasible design map as shown in Figure 6 can be obtained. The green area denotes the feasible design region of core radius and shell thickness to avoid any shell failure. We can observe that the region defines an upper bound of the shell thickness as a function of the core radius. With the parameters used, the maximum shell thickness that can be used is less than ∼0.7 μm. A shell thickness smaller than ∼0.18 μm is able to avoid shell failure for the entire range of core radius from 1 to 5 μm.

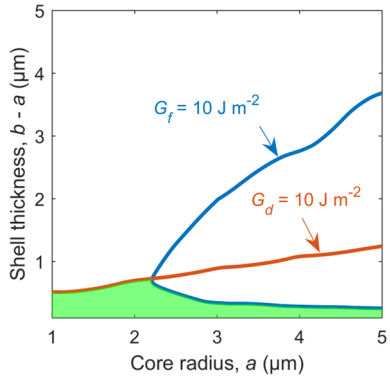

Figure 6. Application of the model for particle design. The green area denotes the feasible design region for the core−shell structure. The smallest shell thickness calculated is 0.1 μm.

DOI: 10.1021/acs.jpcc.7b05096
J. Phys. Chem. C 2017, 121, 19022−19030

4. CONCLUSIONS

In this work, we have developed a model to calculate the lithium concentration and stress inside a particle with the core−shell structure. The diffusion of lithium inside the particle is governed by the gradient of chemical potential, which includes both chemical and mechanical effects. The thermodynamic factor extracted from the open circuit voltage is used to characterize the chemical effect. For the mechanical part, the stress developed in the core−shell structure is calculated using an analogy to thermal stress. As the core and shell are two phases with distinct affinity for lithium, we employ the continuous chemical potential, rather than the continuous lithium concentration, to bridge the core and the shell.

Using this model, we have simulated the mechanical behavior for a particle with a $LiNi_{0.8}Mn_{0.1}Co_{0.1}O_2$ core and a $LiNi_{0.4}Mn_{0.4}Co_{0.2}O_2$ shell. Simulation results reveal that a large tensile tangential stress is generated in the shell during lithiation, while a large tensile radial stress is generated at the core−shell interface during delithiation. These stress states are significantly different from the stress inside a particle of a single component. Using the energy release rate defined in fracture mechanics, we have quantified the effects of core radius, shell thickness, and applied current density on the two failure modes of shell fracture and shell debonding, and constructed a design map. These results can be used to guide the design of core−shell structures.

■ ASSOCIATED CONTENT

Supporting Information

The Supporting Information is available free of charge on the ACS Publications website at DOI: 10.1021/acs.jpcc.7b05096.

Rigorous description of solid diffusion, input parameters, boundary conditions and simulated voltage (PDF)

■ AUTHOR INFORMATION

Corresponding Author

*E-mail: weilu@umich.edu.

ORCID

Bin Wu: 0000-0002-2614-0736

Wei Lu: 0000-0002-4851-1032

Notes

The authors declare no competing financial interest.

■ ACKNOWLEDGMENTS

We are grateful for the support from the National Science Foundation through grant CNS-1446117.

■ REFERENCES

(1) Su, L.; Jing, Y.; Zhou, Z. Li Ion Battery Materials with Core-Shell Nanostructures. *Nanoscale* **2011**, *3*, 3967−3683.

(2) Sun, Y. K.; Chen, Z.; Noh, H. J.; Lee, D. J.; Jung, H. G.; Ren, Y.; Wang, S.; Yoon, C. S.; Myung, S. T.; Amine, K. Nanostructured High-Energy Cathode Materials for Advanced Lithium Batteries. *Nat. Mater.* **2012**, *11*, 942−947.

(3) Sun, Y. K.; Myung, S. T.; Kim, M. H.; Prakash, J.; Amine, K. Synthesis and Characterization of $Li[(Ni_{0.8}Co_{0.1}Mn_{0.1})_{0.8}(Ni_{0.5}Mn_{0.5})_{0.2}]O_2$ with the Microscale Core-Shell Structure as the Positive Electrode Material for Lithium Batteries. *J. Am. Chem. Soc.* **2005**, *127*, 13411−13418.

(4) Ng, S. H.; Wang, J.; Wexler, D.; Chew, S. Y.; Liu, H. K. Amorphous Carbon-Coated Silicon Nanocomposites: A Low-Temperature Synthesis via Spray Pyrolysis and Their Application as High-Capacity Anodes for Lithium-Ion Batteries. *J. Phys. Chem. C* **2007**, *111*, 11131−11138.

(5) Gao, P.; Fu, J.; Yang, J.; Lv, R.; Wang, J.; Nuli, Y.; Tang, X. Microporous Carbon Coated Silicon Core/Shell Nanocomposite via in Situ Polymerization for Advanced Li-Ion Battery Anode Material. *Phys. Chem. Chem. Phys.* **2009**, *11*, 11101−11105.

(6) Laresgoiti, I.; Kabitz, S.; Ecker, M.; Sauer, D. U. Modeling Mechanical Degradation in Lithium Ion Batteries During Cycling: Solid Electrolyte Interphase Fracture. *J. Power Sources* **2015**, *300*, 112−122.

(7) Hao, F.; Fang, D. N. Diffusion-Induced Stresses of Spherical Core-Shell Electrodes in Lithium-Ion Batteries: The Effects of the Shell and Surface/Interface Stress. *J. Electrochem. Soc.* **2013**, *160*, A595−A600.

(8) Kim, H.; Cho, J. Superior Lithium Electroactive Mesoporous Si@Carbon Core-Shell Nanowires for Lithium Battery Anode Material. *Nano Lett.* **2008**, *8*, 3688−3691.

(9) Zhang, X.; Shyy, W.; Marie Sastry, A. Numerical Simulation of Intercalation-Induced Stress in Li-Ion Battery Electrode Particles. *J. Electrochem. Soc.* **2007**, *154*, A910−A916.

(10) Wu, B.; Lu, W. Mechanical-Electrochemical Modeling of Agglomerate Particles in Lithium-Ion Battery Electrodes. *J. Electrochem. Soc.* **2016**, *163*, A3131−A3139.

(11) Sun, Y. K.; Myung, S. T.; Shin, H. S.; Bae, Y. C.; Yoon, C. S. Novel Core-Shell-Structured $Li[(Ni_{0.8}Co_{0.2})_{0.8}(Ni_{0.5}Mn_{0.5})_{0.2}]O_2$ via Coprecipitation as Positive Electrode Material for Lithium Secondary Batteries. *J. Phys. Chem. B* **2006**, *110*, 6810−6815.

(12) Deshpande, R. D.; Bernardi, D. M. Modeling Solid-Electrolyte Interphase (SEI) Fracture: Coupled Mechanical/Chemical Degradation of the Lithium Ion Battery. *J. Electrochem. Soc.* **2017**, *164*, A461−A474.

(13) Jia, Z.; Liu, W. K. Analytical Model on Stress-Regulated Lithiation Kinetics and Fracture of Si-C Yolk-Shell Anodes for Lithium-Ion Batteries. *J. Electrochem. Soc.* **2016**, *163*, A940−A946.

(14) Zhao, K. J.; Pharr, M.; Hartle, L.; Vlassak, J. J.; Suo, Z. G. Fracture and Debonding in Lithium-Ion Batteries with Electrodes of Hollow Core-Shell Nanostructures. *J. Power Sources* **2012**, *218*, 6−14.

(15) Di Leo, C. V.; Rejovitzky, E.; Anand, L. Diffusion-Deformation Theory for Amorphous Silicon Anodes: The Role of Plastic Deformation on Electrochemical Performance. *Int. J. Solids Struct.* **2015**, *67−68*, 283−296.

(16) Takahashi, K.; Higa, K.; Mair, S.; Chintapalli, M.; Balsara, N.; Srinivasan, V. Mechanical Degradation of Graphite/PVDF Composite Electrodes: A Model-Experimental Study. *J. Electrochem. Soc.* **2016**, *163*, A385−A395.

(17) Cui, Z. W.; Gao, F.; Qu, J. M. A Finite Deformation Stress-Dependent Chemical Potential and Its Applications to Lithium Ion Batteries. *J. Mech. Phys. Solids* **2012**, *60*, 1280−1295.

(18) Gao, Y. F.; Cho, M.; Zhou, M. Stress Relaxation through Interdiffusion in Amorphous Lithium Alloy Electrodes. *J. Mech. Phys. Solids* **2013**, *61*, 579−596.

(19) Wan, T. H.; Ciucci, F. Continuum Level Transport and Electro-Chemo-Mechanics Coupling—Solid Oxide Fuel Cells and Lithium Ion Batteries. *Electro-Chemo-Mechanics of Solids* **2017**, 161−189.

(20) Zhao, K. J.; Pharr, M.; Cai, S. Q.; Vlassak, J. J.; Suo, Z. G. Large Plastic Deformation in High-Capacity Lithium-Ion Batteries Caused by Charge and Discharge. *J. Am. Ceram. Soc.* **2011**, *94*, S226−S235.

(21) Bohn, E.; Eckl, T.; Kamlah, M.; McMeeking, R. A Model for Lithium Diffusion and Stress Generation in an Intercalation Storage Particle with Phase Change. *J. Electrochem. Soc.* **2013**, *160*, A1638−A1652.

(22) Guo, M.; Sikha, G.; White, R. E. Single-Particle Model for a Lithium-Ion Cell: Thermal Behavior. *J. Electrochem. Soc.* **2011**, *158*, A122.

(23) Julien, C.; Mauger, A.; Zaghib, K.; Groult, H. Optimization of Layered Cathode Materials for Lithium-Ion Batteries. *Materials* **2016**, *9*, 595.

(24) Xiong, X. H.; Ding, D.; Wang, Z. X.; Huang, B.; Guo, H. J.; Li, X. H. Surface Modification of $LiNi_{0.8}Co_{0.1}Mn_{0.1}O_2$ with Conducting Polypyrrole. *J. Solid State Electrochem.* **2014**, *18*, 2619−2624.

(25) Wei, Y.; et al. Kinetics Tuning of Li-Ion Diffusion in Layered $Li(Ni_xMn_yCo_z)O_2$. *J. Am. Chem. Soc.* **2015**, *137*, 8364−8367.

DOI: 10.1021/acs.jpcc.7b05096
J. Phys. Chem. C 2017, 121, 19022−19030

(26) Lim, J. M.; Hwang, T.; Kim, D.; Park, M. S.; Cho, K.; Cho, M. Intrinsic Origins of Crack Generation in Ni-Rich $LiNi_xMn_yCo_zO_2$ Layered Oxide Cathode Material. *Sci. Rep.* **2017**, *7*, 39669.
(27) Whittingham, M. S. Lithium Batteries and Cathode Materials. *Chem. Rev.* **2004**, *104*, 4271−4301.
(28) Sun, H.; Zhao, K. Electronic Structure and Comparative Properties of Linixmnycozo2 Cathode Materials. *J. Phys. Chem. C* **2017**, *121*, 6002−6010.

DOI: 10.1021/acs.jpcc.7b05096
J. Phys. Chem. C 2017, 121, 19022−19030